Probing redox properties of extreme concentrations relevant for non-aqueous redox-flow batteries

Nathan Stumme,[1] Anton Sameera Perera,[2] Andrew Horvath,[1] Sashen Ruhunage,[2] Darby H. Duffy,[1] Elise M. Koltonowski,[1] Jackson Tupper,[1] Chad Dzierba,[3] Alie D. McEndaffer,[3] Craig M. Teague,[3] Chad Risko[2*] & Scott K. Shaw[1*]

[1]*Department of Chemistry, University of Iowa, Iowa City, Iowa 52242 USA*

[2]*Department of Chemistry & Center for Applied Energy Research, University of Kentucky, Lexington, Kentucky 40506 USA*

[3]*Department of Chemistry, Cornell College, Mount Vernon, Iowa 52314 USA*

Abstract

Redox-flow batteries are an emerging energy storage technology that can pair with intermittent renewable energy technologies. There remains a need, however, to understand physicochemical relationships among the solvent, electrolyte salt, and redox-active molecules that comprise catholyte and anolyte solutions. To examine this relationship, we detail a systematic study wherein the concentrations of the redox-active molecule 2,2,6,6-tetramethylpiperidine 1-oxyl (TEMPO) and $TBAPF_6$ electrolyte salts are varied over concentrations of 1 mM to over 1000 mM in acetonitrile. Three series were investigated: 1) varying the concentration of TEMPO while holding the concentration of $TBAPF_6$ constant, 2) varying the concentration of $TBAPF_6$ while holding the concentration of TEMPO constant, and 3) varying both the concentration of TEMPO and $TBAPF_6$ with a 5:1 $TBAPF_6$:TEMPO ratio. Cyclic voltammetry data from macro- and microelectrodes were used to quantify diffusion coefficients and heterogeneous electron transfer rates, and these metrics were connected to the conductivity and viscosity to develop clear trends over the entire concentration range. Fundamental chemical interactions that lead to changes in physical properties were implicated via vibrational spectroscopy and molecular dynamics (MD) simulations. Trends in conductivity and viscosity for systems were inversely related and correlated to trends in diffusion coefficients and heterogeneous electron transfer rates. Intuitively, faster diffusion and electron-transfer rates occurred with lower TEMPO concentrations and higher $TBAPF_6$ concentrations, with the majority of conditions falling in the general proximity of literature values (k^0 = 0.1-0.5 cm/sec, D = ~2.0-4.0 x 10^{-5} cm^2/sec). At the highest $TBAPF_6$ concentrations, vibrational spectroscopy and MD simulations show that intermolecular interactions were more nuanced, and solvation and ion-pairing effects begin to influence electrochemical and physical properties. This functional approach including electrochemical and physical characterization paired with MD simulations provides a template for methodically studying systems for redox flow battery applications.

Keywords: Non-aqueous redox flow batteries, energy storage, organic redox-active molecules, intermolecular interactions, molecular dynamics, vibrational spectroscopy

Introduction

Increased production from installed solar and wind energy sources has increased the demand for high-capacity and long-term energy storage options. Redox-flow batteries (RFB) have potential to meet this demand,[1] as RFB store energy in electroactive species contained in liquid electrolytes, allowing facile charging and discharging via redox processes.[2] RFB offer decoupled energy density and power density, which can be independently modified by adjusting electrolyte tank volumes and electrode sizes, respectively. This flexibility makes the position of RFB on a standard Ragone plot, which normalizes power and energy density of various energy storage technologies, to be flexible, and that flexibility is highly desirable for developing next-generation electrical power grids.[3]

A wide variety of RFB have been developed with both organic and inorganic redox-active species. Inorganic vanadium RFB that use multiple oxidation states of vanadium oxide as the catholyte and anolyte show great viability and have been developed commercially.[4] Some challenges for vanadium RFB include required thermal regulation to avoid vanadium precipitation as well as vanadium scarcity and metal waste generation. Organic RFB are attractive from a sustainability perspective, and they offer more opportunities to tune redox potential via synthetic design and modification of the redox-active molecules. Some of the most heavily studied and promising organic molecules explored as catholyte and anolyte include nitrobenzene, derivatized methyl viologens, 2,2,6,6-tetramethylpiperidine *N*-oxyl (TEMPO), derivatized quinones, dimethoxybenzenes, benzothiadizoles, and phenothiazines.[5-10]

While organic RFB offer more tunability than their inorganic counterparts, the solubility of their redox-active cores can be strongly dependent on the state of charge of the molecule. Additionally, precipitation of redox-active species and electrolyte can often occur at high concentrations. Maximizing RFB energy and power density primarily relies on increasing the concentration of redox-active species (RAS) while maintaining suitable viscosity, diffusion, and electron transfer kinetics.[2] This necessitates solvent-electrolyte systems that can support conductivity at high salt and RAS concentrations while minimizing the

deleterious effects of increasing viscosity. Generally, supporting electrolyte concentrations are present in concentrations at least 5-10x larger than the RAS to mitigate resistance and migration effects.[11] Systematic electrochemical studies on the impact of analyte and supporting electrolyte concentration have been performed on systems outside the realm of RFB. Work by Vullev and coworkers highlight the dependence of supporting electrolyte concentration on redox potential and peak splitting of ferrocene, a well-known redox probe used as a standard in electrochemisty.[12] As supporting electrolyte concentration was increased, peak splitting narrowed and oxidation potentials shifted considerably to more negative values, suggesting faster kinetics and favorable thermodynamics for the electron transfer. This general concentration dependence concept was expanded to operating RFB, as well. Kosswattaarachchi and Cook investigated battery performance parameters for non-aqueous electrolyte combinations of ferrocene/TEMPO as catholyte and hexafluorophosphate/*N*-methylphthalimide as anolyte in concentration combinations ranging from 10 mM to 1M.[13] Because RFB operate at conditions typically much higher than the dilute conditions often studied by voltammetric analysis, the study of electron-transfer parameters over wide concentration ranges is worthy of thorough systematic investigation in the context of RFB. Clearly defined analytical methodologies to accurately measure these parameters (focusing on operating concentrations $\geq$ 100 mM) will be important for optimizing redox-active species and solvent systems for RFB applications.

Herein, we explore the electrochemistry of TEMPO, a promising and well-known stable aminoxyl radical used as the redox-active molecule in RFB catholytes. The TEMPO radical undergoes electrochemical oxidation to generate $TEMPO^+$, an oxoammonium species that can be reduced back to TEMPO. The reversible electron transfer exhibits a positive redox potential and fast electron-transfer kinetics, all advantageous properties for a RFB catholyte.[14, 15] The first electrochemical characterization of TEMPO dates back to the 1970s by Tamura and coworkers.[16] Since then, TEMPO has been used as a catholyte in a variety of both aqueous and non-aqueous RFB systems.[17-19] Recent approaches have expanded to investigate a variety of TEMPO derivatives as well as the incorporation of ionic liquid as the supporting electrolyte. Outcomes from work by Izgorodina and coworkers showed that the redox potential of TEMPO

can be changed through both derivatizing the molecule itself as well as using different ionic liquids as supporting electrolytes.[20-22] As new combinations are explored with TEMPO, analytical methodologies that can measure relevant electrochemical parameters at battery operating concentrations will provide insight into the viability of emerging systems.

We report electrochemical and physical studies for a series of systematic variations of TEMPO and tetrabutylammonium hexafluorophosphate ($TBAPF_6$) concentrations in acetonitrile. Diffusion coefficients and heterogeneous electron transfer rates are calculated across all concentration conditions with both a macroelectrode and microelectrode. These data are interpreted with corresponding molecular dynamics (MD) simulations, conductivity and viscosity measurements, and vibrational spectroscopy to provide quantitative data on the TEMPO system at a range of concentrations. We also provide guidance on optimal analytical methods to measure electrochemical parameters over large concentration ranges, and specifically higher than the typical 100 mM upper limit. Our results and insights on this system and the methods applied can be expanded to improve understanding of other redox-active species and electrolyte systems that would be used in RFB.

Experimental and Computational Methods

Solution Preparation

Solutions were prepared on the benchtop with an analyte of 2,2,6,6-tetramethylpiperidine *N*-oxyl (TEMPO) (Aldrich>98%) and an electrolyte of tetrabutylammonium hexafluorophosphate $TBAPF_6$ (Aldrich ≥ 99.0%) in acetonitrile (MeCN). The MeCN was dried and degassed with a Pure Process Technologies Solvent Purification System and water content < 1000 ppm for all solutions was verified by a Metraohm 831 Karl Fischer Coulometric Titrator. Stock solutions were prepared for the highest concentration for each series, and dilution was performed to prepare subsequent solutions. For the highest stock concentrations of $TBAPF_6$, sonication was used to dissolve all solid.

Conductivity

Conductivity experiments were performed on a Mettler Toledo SevenCompact S230 Conductivity meter. A three-point calibration was performed with the conductivity probe with Conductivity Standards (Aldrich) prior to obtaining measurements. The electrode was rinsed with acetonitrile and completely dried between measurements.

Viscosity

Viscosity measurements were taken on a Brookfield cone and plate DV2T-LV Viscometer with a TC-550 Temperature Control Circulating bath. Measurements were acquired at 25°C with a CPA-40Z spindle.

Cyclic voltammetry

Cyclic voltammetry (CV) was performed on the benchtop in air-tight, 3-electrode cells connected to a CH Instruments CHI660D potentiostat. Experiments were carried out with an analyte of 2,2,6,6-tetramethylpiperidine *N*-oxyl (TEMPO) (Aldrich>98%) and an electrolyte of tetrabutylammonium hexafluorophosphate $TBAPF_6$ (Aldrich ≥ 99.0%) in acetonitrile (MeCN), which was dried and degassed with a Pure Process Technologies Solvent Purification System. Water content < 1000 ppm was verified by a Metraohm 831 Karl Fischer Coulometric Titrator. The electrochemical cell included a platinum working electrode (d = 2 mm) (CHI102) or platinum working ultramicroelectrode (diameter = 10 μm) (CHI107), a non-aqueous Ag/Ag^+ reference electrode (CHI112) filled with the supporting electrolyte, and a platinum coil counter electrode (99.999% metals basis, Alfa Aesar). The platinum working electrodes were mechanically polished in an aqueous slurry of 1.0 μm followed by 0.3 μm alumina powder on microcloth PSA pads (Buehler). Between grit sizes, the electrodes were sonicated for five minutes in ultrapure water (Milli-Q Advantage A10 system, 18.2 MΩ/cm, TOC < 3 ppb). The platinum counter electrode was flame polished in a hydrogen flame (Linde UHP H_2 99.999%) before each use. All potentials are reported versus the non-aqueous Ag/Ag^+ redox couple. In-depth details for electrochemical methods used to calculate diffusion coefficients and heterogeneous electron-transfer kinetics for macroscopic electrodes and ultramicroelectrodes is contained in the Supplementary Information (SI).

Attenuated total reflectance-Fourier transform infrared spectroscopy ATR-FTIR

A Thermo-Nicolet iS50 Fourier transform spectrometer with liquid N_2 cooled MCT-A detector and PIKE MIRacle ATR attachment with ZnSe crystal was used to acquire FTIR spectra. For ATR measurements, a ca. 200 μL aliquot of the sample was deposited on the ZnSe crystal and held in place via a fluid retaining ring. Spectra were averaged over 32 scans at 4 cm^{-1} resolution. Duplicate spectra were obtained for each sample. The ZnSe crystal was cleaned using copious ultrapure ethanol rinses and allowed to dry under ambient conditions between measurements.

Molecular dynamics (MD) Simulations

Molecular dynamics (MD) simulations were performed for select TEMPO-electrolyte concentrations with the TEMPO in either the neutral or positive (+1) state of charge. Initial simulation configurations were generated using Packmol[23] with a box with the size of 102.0×102.0×102.0 $Å^3$. The numbers of molecules for the simulations at different concentrations are noted in **Table S4**. All MD simulations were carried out using GROMACS 2020 software package.[24] The OPLS-AA (optimized potential for liquid simulations – all atom)[25] forcefield was used for the simulations, and parameters were defined using the LigParGen server[26] and literature.[27] Molecular geometries and electrostatic potential (ESP)-derived partial charges were obtained from density functional theory (DFT) calculations at the ωB97XD/aug-cc-PVDZ level of theory using the CPCM implicit solvation model[28, 29] with MeCN as the solvent, as implemented in the Gaussian 16 software suite.[30] Partial charges were scaled by a factor of 0.8 to compensate for the charge screening effects that are not captured through non-polarizable forcefields such as OPLS-AA.[31] This scaling reproduces the experimental density of these systems to within 1% error.

The simulated systems were initially subject to energy minimization with the steepest descent algorithm up to 100,000 steps followed by a 500 ps simulation under NVT (constant number of molecules, volume, and temperature) conditions with 1 fs time steps using velocity rescaling with a stochastic term to control the temperature at 298.15 K with a 0.1 ps coupling constant.[32] Two simulations under an NPT (constant number of molecules, pressure, and temperature) ensemble were performed, the first applying the Berendsen[33]

pressure coupling for 30 ns to equilibrate the system and the second applying the Parrinello-Rahman[34] pressure coupling for 50 ns. Time steps of 2 fs were used, and the same temperature parameters as mentioned above were used. All NPT simulations used for data collection were performed in triplicate. A further 10 ns NVT simulation with 1 fs timesteps without any bond constraints was performed and velocities at every 2 fs were collected to obtain velocity autocorrelation values to calculate the vibrational density of states.

Given that properties such as viscosity are macroscopic, it is essential that the model systems are large enough and simulation timescales are sufficiently long to capture these effects when using classical MD. Forcefield parameterization plays an important role in the credibility of results, since electrons are not explicitly included in the calculation. Preliminary validation of the forcefield parameters used here included calculating densities of the equilibrated systems at NPT conditions that were comparable to the experimental densities as shown in **Table S5.** Numerical values and trends of viscosity were compared to experimentally derived values of the TEMPO-electrolyte systems at different concentrations, as discussed below**.** Further details on the MD methods, including periodic boundary conditions, visual comparison of all calculated vs experimental properties **(Figure S49),** and additional analyses are available as SI.

Results and Discussion

TEMPO was chosen as the redox probe for this work due to well-established electrochemical behavior and applicability to RFB. The organic solvent acetonitrile and non-aqueous electrolyte $TBAPF_6$ were selected because they are commonly used for electrochemical analyses and are electrochemically inert within the potential window required for these studies. To provide a comprehensive study of concentration conditions, three unique series of solution conditions were investigated: **1**) varying the concentration of TEMPO while holding the concentration of $TBAPF_6$ constant, **2**) varying the concentration of $TBAPF_6$ while holding the concentration of TEMPO constant, and **3**) varying both the concentration of TEMPO and $TBAPF_6$ with a 5:1 ratio of $TBAPF_6$ to TEMPO. **Table 1** lists each concentration condition measured, along with molar

ratios of solutes (TEMPO, TBA^+, and PF_6^-) to solvent (acetonitrile)**.** When determining molar ratios, the TBA^+ and PF_6^- were considered as independent ions. Presenting molar ratios enables comparison between experimental electrochemical data, physical trends, and solvation.

Bulk solution properties of conductivity and viscosity were characterized at each concentration condition and values for each series are plotted as a function of mole ratio in **Figure 1** with supporting molecular dynamics (MD) simulation data in **Table 2** and **Table 3**. Trends in conductivity (**Figure 1,** top) largely depend on changing the concentration of $TBAPF_6$, with higher concentrations of supporting electrolyte generally leading to higher conductivity values (conditions **2** and **3**). At the highest concentrations of supporting electrolyte, which is ~1000 mM or 0.1 mol ratio solute-to-solvent, there is a plateau around 28 mS/cm followed by a decrease in conductivity. MD simulations reasonably reproduce numerically the measured conductivities, as general conductivity trends as a function of concentration were captured, including the plateau region followed by a decrease in conductivity. Capturing these trends serves as an important validation of the theoretical approach (**Table 3).**

The plateau in conductivity is attributed to decreased transport velocity of ions at high concentrations, effects of ionic association, and solvation. At high electrolyte concentrations, oppositely charged ions can become forced into close contact and undergo ion pairing, which effectively neutralizes the solution and inhibits electrical conductivity, resulting in the plateau.[35] The conductivity does still remain relatively high in these cases due to the high concentration of $TBAPF_6$ present, which provides ample ions to conduct charge despite this ion pairing effect.

Results from MD simulations confirm that impaired ion movement is likely the cause of the inhibition of the solution conductivity at higher $TBAPF_6$ concentrations. As the numbers of TBA^+ ions increase, clusters are observed to form in the simulations that have large amounts of TBA^+. Notably, these clusters have different relative sizes as a function of the concentrations of the solution components. When the concentrations of TBA^+ (TEMPO:$TBAPF_6$ = 50 mM:1000 mM) or $TEMPO^+$ (TEMPO:$TBAPF_6$ = 1000

mM:100 mM) are large, these clusters are relatively small in size (≈10 Å radius) and contain large numbers of TBA^+ or $TEMPO^+$ molecules, respectively. On the other hand, with smaller TBA^+ or TEMPO concentrations (TEMPO:$TBAPF_6$ = 50:500, 100:100, 200:200), larger clusters are formed, and these clusters are less dense **[Figure S54 (iii),(iv)]**. These clusters are discussed in further detail below. It is worth noting that observations of depreciating conductivity at high supporting electrolyte concentrations have been reported in other similar systems.[36]

Changes in the concentration of TEMPO alone (condition **1**) have relatively small impact on the conductivity, with marginal decreases in conductivity with increasing concentrations of TEMPO. For these conditions, we hypothesize that ionic association and solvation effects could be less prominent due to smaller and consistent electrolyte concentrations; additionally, the mol ratio of these solutions is also smaller due to the relative molecular weight of TEMPO to $TBAPF_6$.

MD simulations also suggest that at larger concentrations of $TBAPF_6$, the conductivity declines with TEMPO oxidation. In contrast, at larger concentrations of TEMPO, charged systems show the opposite effect, with conductivity increasing with the TEMPO concentration **(Table S8)**. This trend generally aligns well with the plateauing of experimental conductivities at high $TBAPF_6$ concentrations. Given that experimental data was conducted on neutral TEMPO, the plateauing phenomenon could possibly be exacerbated in an operating RFB setup when the oxidation of TEMPO occurs. Estimated bulk diffusivity values **(Table S10)** also indicate a decline in diffusivity in charged systems when compared to neutral systems.

Turning to the viscosity, the trends are significantly affected by $TBAPF_6$ concentration but marginally affected by TEMPO concentration (**Figure 1,** bottom). There is an increase in viscosity as the concentration of $TBAPF_6$ is increased, particularly at the highest concentrations of supporting electrolyte (conditions **2** and **3**). Like trends in conductivity, changes in the concentration of TEMPO alone (condition **1**) have a small impact on viscosity. Comparing viscosity and conductivity, a relationship between the two emerges,

particularly in the impact of the concentration of $TBAPF_6$ on each parameter. The rise in viscosity with increasing concentration of $TBAPF_6$ corresponds directly with the plateau and drop in conductivity at the highest concentrations of supporting electrolyte. This supports that the movement of ions is likely impaired at high electrolyte concentrations, inhibiting the overall solution conductivity. This is consistent with the Walden rule, whereby molar conductivity and viscosity are inversely related as well as the Stokes-Einstein relation for the diffusion of charged particles with applied forces.[37] Interestingly, the concentration of $TBAPF_6$ largely dictates both conductivity and viscosity trends relative to the concentration of TEMPO, implying that changes to supporting electrolyte concentration are significantly more impactful to solution physical properties. As previously mentioned, the molecular weight of $TBAPF_6$ is roughly 2.5x greater than TEMPO, which leads to more atoms and mass being present at a given concentration. This, in combination with the role electrolyte plays in impacting conductivity, could explain this observation.

MD simulations reasonably predict the numerical values and capture the viscosity trends observed experimentally for the neutral TEMPO solutions. However, at larger simulated electrolyte concentrations (TEMPO:$TBAPF_6$ = 50 mM:1000 mM), the numerical viscosity predictions deviate substantially from experimental values. In systems where the contribution of finite size effects is significant and due to the crowding of the electrolytes, the hydrodynamic behavior of the solutions can be affected.[38-41] The behavior of viscosity vs k-vectors shows a deviation from the expected symmetric third-order polynomial fit function used in the transverse current autocorrelation method as the solutions diverge from a dilute liquid to a thicker fluid.[42] Plots of viscosity (η) vs k-vector (**Figures S49-50**) were extrapolated to k = 0 (k is the wave vector of the fluctuation) to obtain macroscopic viscosity. As observed experimentally, the viscosity of these solutions is significantly affected by the concentration of the electrolyte rather than TEMPO. The number of $TBAPF_6$ molecules shows a linear relationship with both experimental and calculated viscosities, whereas such a relationship between the number of TEMPO molecules is not observed **(Figure S52)**. When compared to neutral systems, the calculated viscosities show that charged TEMPO solutions are more viscous, possibly due to the stronger solvent/solute and solute/solute intermolecular interactions facilitated

by the electrostatic contribution from the TEMPO charge **(Table S7).** Like conductivity before, this would have implications in an operating RFB.

Electrochemical cyclic voltammetry (CV) measurements at three representative concentrations for each solution condition are shown in **Figure 2.** All scan-rate dependent CVs are shown in **SI Figures S1-S22**. Several qualitative trends are apparent from the CV data. As the concentration of TEMPO increases (**Figure 2,** top), there is a simultaneous increase in peak current and peak splitting, corresponding to more TEMPO diffusing to the electrode surface and accompanying slower electron transfer kinetics at higher concentrations of TEMPO, respectively.[43, 44] In contrast, as the concentration of $TBAPF_6$ increases (**Figure 2,** middle), we observe a decrease in peak splitting, corresponding to the increased conductivity of the electrolyte. Interestingly, there is also a decrease in the peak current at the highest concentrations of supporting electrolyte. This decrease in peak current suggests impaired diffusion of TEMPO with high concentrations of $TBAPF_6$, which is consistent with viscosity trends shown in **Figure 1**. Changing both the concentration of TEMPO and $TBAPF_6$ together in a fixed ratio (**Figure 2,** bottom) results in an increase in peak current and peak splitting. This trend is similar to condition **1** in which the concentration of TEMPO is increased; however, in condition **3** the increase in peak current and splitting is less pronounced because the concentration of $TBAPF_6$ is scaling alongside the increase in the concentration of TEMPO.

Diffusion coefficients (D) and heterogeneous electron transfer rates (k^0) based on CV data were calculated. Calculations were based on the Randles–Ševčík equation, the Nicholson method, or a simulation fitting a regression of $\frac{k^0}{\sqrt{D}}$ with ΔE_p to calculate k^0 depending on the magnitude of peak splitting values. Complete details for each method are contained in the SI.

Anodic and cathodic diffusion coefficients calculated from 2 mm diameter electrode CV data are shown in **Figure 3** and are plotted as a function of molar ratio of both TEMPO and $TBAPF_6$ to acetonitrile. **Table 1** contains the calculated molar ratio values for each concentration condition. In condition **1** as the concentration of TEMPO is increased (**Figure 3**, top left), the diffusion coefficient decreases with

increasing TEMPO concentration. At the smallest concentration of TEMPO in **1** (1 mM), the measured diffusion coefficient value matches well to values obtained for TEMPO in literature (~2.0-4.0 x 10^{-5} cm^2/sec).[45] In condition **2** when the concentration of $TBAPF_6$ is increased (**Figure 3,** middle left), the diffusion coefficient increases, then plateaus and drops.[45] This plateau in diffusion coefficient is consistent with trends seen for conductivity and viscosity measurements for condition **2.** When the concentration of TEMPO and $TBAPF_6$ are increased together in condition **3 (Figure 3**, bottom left) the diffusion coefficient decreases with larger concentrations of TEMPO and $TBAPF_6$ present.

Heterogeneous electron-transfer rates shown in **Figure 3** provide quantitative values to evaluate the qualitative peak splitting changes previously mentioned. A table of numerical values for each concentration condition is supplied in **Table S1**. For condition **1,** as the concentration of TEMPO increases (**Figure 3,** top right), k^0 decreases rapidly as peak splitting values grow larger. Similar to diffusion coefficient, k^0 for the lowest concentration of TEMPO in condition **1** (1 mM) matches literature value heterogeneous electron transfer rates (~0.1-0.5 cm/sec).[45] In contrast, increasing the concentration of $TBAPF_6$ in condition **2** (**Figure 3,** middle right) leads to an increase in k^0 with additional $TBAPF_6$ present to increase conductivity and promote charge transfer. However, as the highest concentrations of $TBAPF_6$ are reached, k^0 eventually plateaus and begins to drop slightly. Similar to the diffusion coefficient trends, k^0 changes correspond to the observed rise in solution viscosity and plateau in conductivity at high concentrations of $TBAPF_6$. Meanwhile, the gradual increase in peak splitting when the concentration of TEMPO and $TBAPF_6$ are increased together in condition **3** (**Figure 3,** bottom right) leads to a gradual decrease in k^0, which is similar to the trend observed for the diffusion coefficient.

In conditions of low $TBAPF_6$ concentrations and high TEMPO concentrations, we observe irregular CV curves, decreased diffusion coefficients, and heterogeneous electron transfer rates. We attribute these trends in part to undesirable effects of migration and uncompensated resistance when there is insufficient electrolyte concentration or excess analyte concentration. At the higher concentrations of TEMPO, diffusion limited peak-currents in the CV traces have much larger ΔE_{peak} values, a result likely due to the

equilibrium between electrolyzed species generated at the electrode surface and neutral species present in the bulk solution much more strongly favoring the neutral species in the bulk. As a result, it takes longer to deplete neutral species near the electrode at high analyte concentrations, which results in wider peak splitting values and slower k^0 calculations. Additionally, in low electrolyte conditions, migration and uncompensated resistance effects exacerbate peak splitting and limit the amount of current that can be passed. The CVs with peak splitting exceeding 1V between oxidation and reduction features are strongly impacted by each of these factors, and do not provide accurate or quantitative values for D and k^0.

Due to the limitations presented by macroscopic electrodes at extreme concentration ranges, we also collected data using Pt ultramicroelectrodes, which are known to mitigate effects of migration and uncompensated resistance and provide comparison in calculated diffusion coefficient and heterogeneous electron transfer rate values. With an ultramicroelectrode, the current response is mainly dependent on the size of the electrode, and the mode of diffusion is radial rather than planar in the case of macroelectrodes.[44] Because the electrode is so small and passes small amounts of current, uncompensated resistance effects are minimized. The size of the electrode and the mode of diffusion results in a steady-state current response through a wide range of applied scan rates, because the amount of material electrolyzed at the electrode interface is small and can diffuse away quickly without depletion. As such, there is not a diffusion-limited current response like there is for larger electrodes that undergo planar diffusion **(Figure S56)**.[11] Steady-state current equations can be used to calculate both diffusion coefficient and heterogeneous electron transfer rates from microelectrode data through a wide range of concentration conditions.

Using a Pt ultramicroelectrode (diameter = 10 μm), diffusion coefficient and heterogeneous electron-transfer rates were calculated for all concentration conditions. Diffusion coefficients were calculated using the steady-state current equation for a disk microelectrode[9], and heterogeneous electron transfer rates were calculated using the method developed by Oldham.[11, 46] Complete details for each method are contained in the Supplementary Information, and tables of diffusion coefficients and heterogeneous electron transfer rates and CVs for all concentrations are contained in **SI Figures S23-S44.**

Diffusion coefficients measured using the Pt ultramicroelectrode (diameter = 10 μm) are shown in **Figure 4.** It is immediately evident that changes in diffusion coefficients for all cases are more gradual than those observed with the larger 2 mm diameter electrode and more consistent with the diffusion coefficients for TEMPO reported from literature.[45] Specifically, as the concentration of TEMPO is increased across a constant electrolyte concentration (**Figure 4**, top left, condition **1**), measured diffusion coefficients for TEMPO are consistently near literature values, before decreasing at only the highest concentrations of TEMPO (250 mM and higher). [45] This decrease in diffusion coefficient is associated with gradual changes in conductivity and viscosity for condition **1** as shown in **Figure 1**. In condition **2** (changing $TBAPF_6$ concentration, **Figure 4**, middle left) the diffusion coefficient increases slightly with more electrolyte present and then decreases as the largest concentrations (500 mM and higher) of $TBAPF_6$ are reached. Diffusion coefficient values are close to literature values for lower concentrations and then drop slightly at the highest concentrations of $TBAPF_6$. Lastly, in condition **3** where the concentration of TEMPO and $TBAPF_6$ are changed together (**Figure 4**, bottom left), there is a decrease in diffusion coefficient with increasing concentration of redox-active species and supporting electrolyte, with values staying close to literature values throughout the entire concentration range. These trends suggest that diffusion of TEMPO is impaired only at the highest concentrations of redox-active material or electrolyte, with low to intermediate concentrations yielding values similar to what is observed in literature for low concentration systems.

Heterogeneous electron-transfer rates with the ultramicroelectrode also in **Figure 4** follow similar trends to those observed with the 2 mm diameter electrode; however, they span over only one order of magnitude and are more consistent with literature values throughout all concentrations.[45] This is attributed to lower current values and minimized uncompensated resistance effects with the ultramicroelectrode.[45] In condition **1** as the concentration of TEMPO is increased across a constant electrolyte concentration, (**Figure 4**, top right), k^0 values exponentially decrease as more TEMPO is present, staying close to literature values until only the highest concentrations of TEMPO are reached. For condition **2** where the concentration of $TBAPF_6$

is increased with a constant concentration of TEMPO, (**Figure 4**, middle right) there is an increase in k^0 consistent with increased conductivity and charge transfer with more supporting electrolyte, followed by a plateau and decrease in k^0 at the highest concentrations of $TBAPF_6$. Like before, this decrease likely corresponds to the rise in bulk viscosity and decrease in conductivity at the highest concentration of $TBAPF_6$. In condition **3**, there is an exponential decrease in k^0 with more TEMPO and $TBAPF_6$ present, which is consistent with conductivity and viscosity trends. Like condition **1** and **2**, k^0 values for condition **3** reside close to literature values up until the highest concentration conditions.

Trends from Pt ultramicroelectrode diffusion coefficients and heterogeneous electron-transfer rates are consistent with each other, with general decreases to both as the molar ratio of solute:solvent is increased. Changes in these parameters for each condition are also consistent with conductivity and viscosity trends and are more gradual as the ultramicroelectrode mitigates migration and uncompensated resistance effects. Because of this, it is suggested that using an ultramicroelectrode is the optimal approach for characterizing extreme concentration combinations of analyte and supporting electrolyte. Analyzing the data, it appears the definite 'breaking point' (>1V peak splitting) for the macroelectrode system was in condition **1** when the TEMPO concentration exceeded 250 mM and in condition **2** when the $TBAPF_6$ concentration was smaller than 10 mM. This likely stems from the diffusion-limited current response being susceptible to deviation under non-ideal solution conditions (low supporting electrolyte concentration or high analyte concentration).[44]

Emerging trends from electrochemical and physical characterization show that increasing the concentration of TEMPO (condition **1)** leads to marginal increases in viscosity and decreases in conductivity, resulting in decreases to diffusion coefficient and heterogeneous electron transfer rates. Increasing the concentration of $TBAPF_6$ (condition **2**) promotes both increased conductivity and viscosity, facilitating faster diffusion and heterogeneous electron transfer rates until viscosity and conductivity limitations take over at the highest concentrations of $TBAPF_6$ (1000 mM+). Changes to the concentration of $TBAPF_6$ appear to have a larger overall effect on the system, with physical and electrochemical properties tracking largely along with the

concentration of $TBAPF_6$, even when the concentration of TEMPO and $TBAPF_6$ are changed together in a fixed ratio (condition **3**).

Our data shows that the supporting electrolyte plays a large role in influencing the electrochemical and physical properties for these systems. From a conventional electrochemistry context, having excess supporting electrolyte relative to analyte mitigates the impact of charge migration and the undesirable movement of a species due to a potential gradient rather than solely a concentration gradient. While an intuitive approach may be to add as much supporting electrolyte as solubility permits, our data also identifies an upper limit to the benefits of electrolyte and deleterious effects that accompany high supporting electrolyte concentrations including decreased conductivity, increased viscosity, and decreased diffusion and heterogeneous electron transfer rates. This phenomenon has also been observed in other systems[47, 48] whereby the interactions between supporting ions increases at high concentrations, ultimately screening charge and decreasing the molar conductivity. The interplay between these phenomena leads to a critical supporting electrolyte concentration that is unique to each electrolyte species and system. In the context of RFB applications, identifying these critical concentrations for systems and the fundamental chemistry at play will aid the design and tailoring of redox-active materials and supporting electrolytes. Looking at our conductivity data, it appears that this critical electrolyte concentration for TEMPO and $TBAPF_6$ is around 1000 mM $TBAPF_6$ or 0.1 mol ratio solutes:solvent, as the conductivity begins to plateau and decrease at larger electrolyte concentrations than this.

These trends in electrochemical and physical properties at high concentrations of $TBAPF_6$ are likely connected to changes in the solvation of both TEMPO and $TBAPF_6$ by acetonitrile. With the decrease in conductivity and increase in viscosity at these concentrations, the solvation of each species is presumably decreasing, which dictates how freely species can diffuse in solution and how TEMPO can undergo electron transfer. It is likely that at these high electrolyte concentrations, ion pairing interactions are also occurring between TBA^+ and PF_6^- ions because there is insufficient solvent present to solvate the ions. This ultimately inhibits electrical conductivity.[35]

Shedding some light on these experimental observations, RDF of solute and solvent molecules around a reference molecule provided by MD simulations reveal interactions between different components in the solution. These are particularly helpful in identifying important details in crowded electrolyte environments, such as ion association. **Figure 5** summarizes the RDF from the center of mass (COM) of charged TEMPO [**Figure 5(i)**] and PF_6^- [**Figure 5(ii)**] to the COM of other molecules in different solutions simulated. A similar figure for neutral TEMPO systems can be found in the SI (**Figure S53**). When the RDF with respect to TEMPO is considered, the neutral systems do not exhibit defined structuring of any other molecule around TEMPO. However, we observe the structuring of PF_6^- around $TEMPO^+$, suggesting the formation of a solvation shell with PF_6^-, with a coordination number (CN) ranging from 0.5 to 1.7 at a radius of 4.7 Å (RDF peak). The solvent shell behavior extends to almost 10 Å, where up to 11 PF_6^- molecules can be found within a radius of 8.0 Å for the highest solute concentration (TEMPO:$TBAPF_6$ = 1000 mM:100 mM) simulated (**Table 4).** This result is at an approximate molar ratio of 0.06 where heterogeneous electron transfer rate begins to plateau. These MD simulations suggest that, in charged systems, $TEMPO^+$ molecules drift away from each other due to charge repulsion, and $TEMPO^+$ and PF_6^- ions arrange themselves in close vicinity assisted by their opposing charges. Furthermore, ion pair formation is suggested by the nearly identical radial distribution profiles portrayed in **Figure 5(i)** and **Figure 5(ii)** with a CN ≈ 1 **(Table 4)** for the $TEMPO^+/PF_6^-$ complex around the 4.7 Å RDF peak.

Ion pair formation can also be visualized through the average atomic distances between the *N* atom of TEMPO and *P* atom of PF_6^-, where the distance for the charged systems varies from 4.11-4.56 Å. [**Figure** 5 (iii)] Analysis of the number of close contacts (intra-atomic distances < 5Å) reveals that the contacts of *P* atom of PF_6^- with $TEMPO^+$ originates from mostly the *O* atom and then from *N* (**Table S11).** This result is further supported by RDF plots with respect to specific atoms. Characteristics of both solvent-shared ion pairs (SIP) and solvent-separated ion pairs (SSIP) are noted. As suggested by the small bump in the MeCN RDF profile in **Figure 5(ii),** a MeCN solvation shell could form around PF_6^-, surrounding the ion with an average of 15 solvent molecules for all simulated concentrations. However, the value of g(r) reaching a

value of 1.0 in **Figure 5(i)** indicates an evenly distributed MeCN system around $TEMPO^+$. Interestingly, we also observe patterns showing that g(r) for TEMPO:$TBAPF_6$ = 100 mM:100 mM and 200 mM:200 mM are higher compared to systems with higher solute concentrations, suggesting that the strongest structuring (leading to more ion association) of TEMPO/PF_6 occurs in equimolar systems. For both neutral and charged systems, we observe similar MeCN solvation shell behavior and structuring of TBA^+ around PF_6^-. This hints that PF_6^- ions could be surrounded by a shell of TBA^+/MeCN, irrespective of the charge of TEMPO.[49, 50]

To further investigate this effect experimentally, the solvation environment of PF_6^- was explored with vibrational spectroscopy for all solution conditions, and results were compared with MD calculations. **Figure 6** shows the P-F stretching vibration from the PF_6^- anion in the $TBAPF_6$ electrolyte in each of the three conditions.[51] Full spectra corresponding to each of the three conditions can be found in **Figures S45, S46, and S47** in the Supplemental Information.[51] In condition **1** (**Figure 6**, top) where the concentration of $TBAPF_6$ is held constant, there is no shift in vibrational frequency and a very subtle decrease in absorbance as the concentration of TEMPO is increased due to a small amount of PF_6 being displaced by additional TEMPO. **Figure 6** (middle) corresponds to condition **2**, wherein the concentration of TEMPO is held constant and the concentration of $TBAPF_6$ is varied. A significant increase in absorbance is concomitant with increasing concentration, but more interesting is a shift to lower vibrational frequency as the concentration of $TBAPF_6$ is increased. This same shift is also observed in condition **3** (**Figure 6**, bottom) wherein the concentrations of TEMPO and $TBAPF_6$ are both varied but kept in the same ratio relative to each other. **Figure 7** shows plots of the peak shifts (top) and changes in absorbance (bottom) with changing concentration for each of the three conditions, along with a solution containing only $TBAPF_6$ in MeCN. The observed linear trend for the change in vibrational frequency suggests that TEMPO-$TBAPF_6$ interactions have not reached a maximum in this measured concentration range, but the solvent has reached its carrying capacity for solute due to solubility limitations. The whole spectra for $TBAPF_6$ in MeCN can be seen in **Figure S48** in the SI. While the change in vibrational frequency with concentration is observed

to be a linear trend, the change in absorbance appears linear at low concentrations but deviates from linearity at high concentrations.

The shift in the P-F stretching vibration to lower frequencies as the concentration of $TBAPF_6$ is increased implies that the P-F bond is in a more stable chemical environment. This shift with concentration is only observed in the P-F mode, while all other modes in the spectra remain constant. This red shift is not observed in the presence of increasing TEMPO concentration, which suggests that the PF_6^- ion is not strongly interacting with TEMPO in solution. In fact, the frequency shift of the P-F mode is observed in the complete absence of TEMPO (**Figure 7**, top), implying that increasing intermolecular interactions are due to the PF_6^- anion interacting with the TBA^+ cation, acetonitrile, or even possibly a lack of interaction with the solvent. In terms of interaction with the TBA^+ cation, previous work has shown that at high concentrations, ion pairing interactions are observed.[35] These spectroscopic results support the RDF data from the MD simulations and help to begin linking changes in the solvation of ions to changes in viscosity, conductivity, and electrochemical properties.

Fourier-transformed velocity autocorrelation functions derived from MD trajectories were used to estimate vibrational spectroscopic data for these conditions. A vibrational power spectrum that represents vibrational density of states was obtained using this approach, which can be correlated to an IR spectrum. We were able to reproduce three out of four peak regions that were experimentally observed, including the P-F stretching peak region (**Figure S55**). However, the IR peak-shifting of the P-F mode to lower wavenumbers was not captured through this method. The use of dipole autocorrelation instead of velocity autocorrelation yields similar results since the OPLS forcefield used is non-polarizable. Using trajectories from classical MD simulations for this purpose is limited by the intrinsic limitation of classical MD to not capture the quantum effects of nuclear motion which affect absorption intensity, peak shape, etc. More complex methods such as ab initio MD or the application of quantum corrections to autocorrelation functions would improve these results; however, these were deemed too computationally expensive for the purpose of this study.[52, 53]

Conclusions

The findings from this study show how trends in conductivity, viscosity, diffusion coefficient, and heterogeneous electron transfer rate change for varying electrolyte and redox-active species concentrations. Through CV analysis with both a 2 mm diameter electrode and 10 μm diameter ultramicroelectrode, diffusion coefficients and heterogeneous electron transfer rates were determined for all concentration conditions. Electrochemical trends were experimentally connected to physical properties of conductivity and viscosity as well as spectroscopic data to provide a comprehensive understanding of the impact of the concentration of redox-active species and supporting electrolyte on electrochemical performance. Combined with MD simulations, we present a holistic account of the system and provide chemical reasoning for observations, including plausible chemical interactions between molecules.

Our results also highlight the best approaches to measure electrochemical parameters over wide concentration ranges and under conditions that are traditionally difficult to characterize. In agreement with literature precedence, a 10 μm diameter microelectrode is more suitable for non-traditional solution conditions as it can more accurately measure D and k^0 in conditions of low electrolyte concentration and high redox-active species.[11, 46] This performance difference is attributed to the mode of radial diffusion to the electrode surface rather than planar diffusion in the case of larger electrodes. It is worth noting that the 2 mm diameter macroelectrode performed well under more traditional electrochemical conditions of low redox-active species concentration and high electrolyte concentration.

While findings from this work pertain to TEMPO, the general approach of using an ultramicroelectrode to characterize electrochemical parameters over a wide concentration range of redox-active species and supporting electrolyte is applicable to all electroactive species used in RFB. Additionally, trends in conductivity, viscosity, and solvation for concentration ranges track well with electrochemical parameters and could serve as useful characterization for understanding the concentration parameters of chemical systems of interest. Given the wide range of possible electroactive molecules for RFB, the multifaceted

characterization approach defined within this work provides a template for comprehensively analyzing and optimizing systems for RFB applications.

Supporting Information

Additional experimental details, electrochemical, spectroscopic, and computational data and tables are contained in the Supplementary Information.

Corresponding Authors

Scott K. Shaw – Department of Chemistry, The University of Iowa, Iowa City, Iowa 52242, United States. Email: scott-k-shaw@uiowa.edu
Chad Risko – Department of Chemistry, The University of Kentucky, Lexington, Kentucky, 40506, United States. Email: chad.risko@uky.edu

Authors

Nathan C. Stumme – Department of Chemistry, The University of Iowa, Iowa City, Iowa 52242, United States
Anton Perera – Department of Chemistry, The University of Kentucky, Lexington, Kentucky, 40506, United States
Andrew Horvath – Department of Chemistry, The University of Iowa, Iowa City, Iowa 52242, United States
Sashen Ruhunage – Department of Chemistry, The University of Kentucky, Lexington, Kentucky, 40506, United States
Darby Duffy – Department of Chemistry, The University of Iowa, Iowa City, Iowa 52242, United States
Elise Koltonowski – Department of Chemistry, The University of Iowa, Iowa City, Iowa 52242, United States
Jack Tupper – Department of Chemistry, The University of Iowa, Iowa City, Iowa 52242, United States
Craig M. Teague – Department of Chemistry, Cornell College, Mount Vernon, Iowa 52314, United States
Chad Dzierba – Department of Chemistry, Cornell College, Mount Vernon, Iowa 52314, United States
Alie McEndaffer – Department of Chemistry, Cornell College, Mount Vernon, Iowa 52314, United States

Author Contributions

S.K.S and C.R. conceptualized and supervised the work. N.S. completed electrochemical and physical studies and calculations and A.H. completed spectroscopic studies. A.P. and S.R. completed all MD calculations. E.K., J.T., D.D., C.M.T., C.D, and A.M. assisted with electrochemical and spectroscopic experiments. N.S., A.P., S.K.S., and C.R. assembled the manuscript and Supporting Information, and all authors assisted with editing. All authors have given approval to the final version of the manuscript.

Acknowledgments

This work was generously supported by the National Science Foundation under Cooperative Agreement Number 2019574. We gratefully acknowledge Prof. Johna Leddy for helpful discussions in evaluating electrochemical data. We are grateful for the support of glass, electronics, and machine shops support at the University of Iowa, which greatly facilitated this research. We also acknowledge the University of Kentucky (UK) Center for Computational Sciences and Information Technology Services Research Computing for their fantastic support and collaboration, and use of the Lipscomb Compute Cluster and associated research computing resources.

TOC Graphic

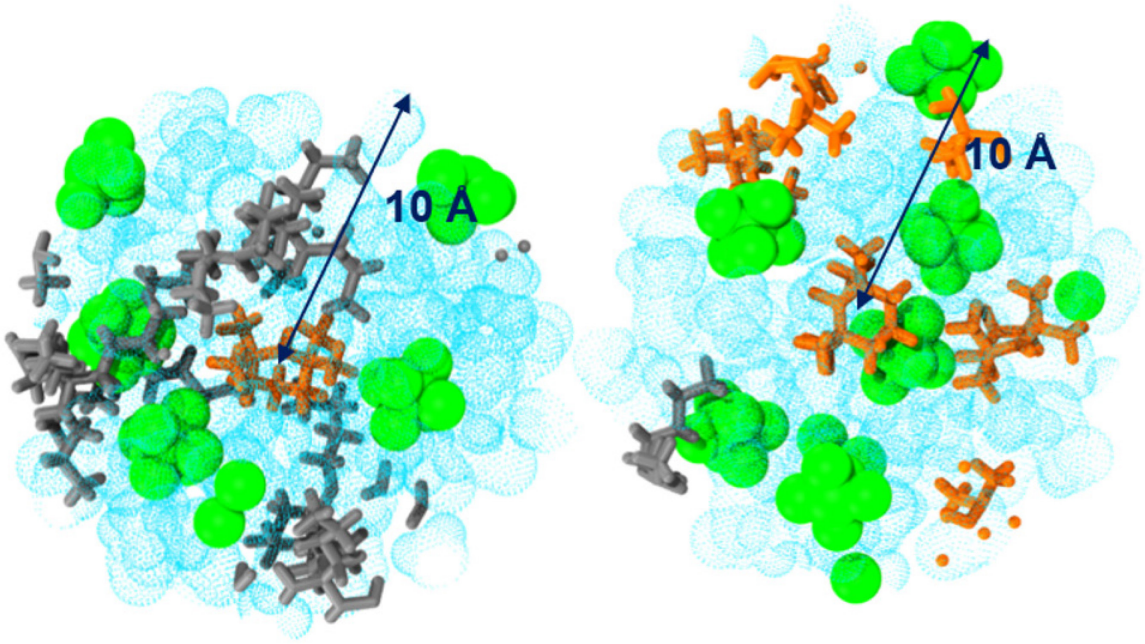

References

Uncategorized References

1. Soloveichik, G. L., Flow Batteries: Current Status and Trends. *Chem Rev* **2015,** *115* (20), 11533-58.
2. Weber, A. Z.; Mench, M. M.; Meyers, J. P.; Ross, P. N.; Gostick, J. T.; Liu, Q., Redox flow batteries: a review. *Journal of Applied Electrochemistry* **2011,** *41* (10), 1137-1164.
3. Pham-Truong, T. N.; Wang, Q.; Ghilane, J.; Randriamahazaka, H., Recent Advances in the Development of Organic and Organometallic Redox Shuttles for Lithium-Ion Redox Flow Batteries. *ChemSusChem* **2020,** *13* (9), 2142-2159.
4. Lourenssen, K.; Williams, J.; Ahmadpour, F.; Clemmer, R.; Tasnim, S., Vanadium redox flow batteries: A comprehensive review. *Journal of Energy Storage* **2019,** *25*, 100844.
5. Zhong, F.; Yang, M.; Ding, M.; Jia, C., Organic Electroactive Molecule-Based Electrolytes for Redox Flow Batteries: Status and Challenges of Molecular Design. *Front Chem* **2020,** *8*, 451.
6. Li, Z.; Lu, Y. C., Material Design of Aqueous Redox Flow Batteries: Fundamental Challenges and Mitigation Strategies. *Adv Mater* **2020,** *32* (47), e2002132.
7. Li, M.; Odom, S. A.; Pancoast, A. R.; Robertson, L. A.; Vaid, T. P.; Agarwal, G.; Doan, H. A.; Wang, Y.; Suduwella, T. M.; Bheemireddy, S. R.; Ewoldt, R. H.; Assary, R. S.; Zhang, L.; Sigman, M. S.; Minteer, S. D., Experimental Protocols for Studying Organic Non-aqueous Redox Flow Batteries. *ACS Energy Letters* **2021**, 3932-3943.
8. Attanayake, N. H.; Kowalski, J. A.; Greco, K. V.; Casselman, M. D.; Milshtein, J. D.; Chapman, S. J.; Parkin, S. R.; Brushett, F. R.; Odom, S. A., Tailoring Two-Electron-Donating Phenothiazines To Enable High-Concentration Redox Electrolytes for Use in Nonaqueous Redox Flow Batteries. *Chemistry of Materials* **2019,** *31* (12), 4353-4363.
9. Huang, J.; Pan, B.; Duan, W.; Wei, X.; Assary, R. S.; Su, L.; Brushett, F. R.; Cheng, L.; Liao, C.; Ferrandon, M. S.; Wang, W.; Zhang, Z.; Burrell, A. K.; Curtiss, L. A.; Shkrob, I. A.; Moore, J. S.; Zhang, L., The lightest organic radical cation for charge storage in redox flow batteries. *Sci Rep* **2016,** *6*, 32102.
10. Duan, W.; Huang, J.; Kowalski, J. A.; Shkrob, I. A.; Vijayakumar, M.; Walter, E.; Pan, B.; Yang, Z.; Milshtein, J. D.; Li, B.; Liao, C.; Zhang, Z.; Wang, W.; Liu, J.; Moore, J. S.; Brushett, F. R.; Zhang, L.; Wei, X., "Wine-Dark Sea" in an Organic Flow Battery: Storing Negative Charge in 2,1,3-Benzothiadiazole Radicals Leads to Improved Cyclability. *ACS Energy Letters* **2017,** *2* (5), 1156-1161.
11. A. Bard, L. F., *Electrochemical Methods Fundamentals and Applications*. John Wiley & Sons: United States, 2001; Vol. 2, p 833.
12. Bao, D.; Millare, B.; Xia, W.; Steyer, B. G.; Gerasimenko, A. A.; Ferreira, A.; Contreras, A.; Vullev, V. I., Electrochemical Oxidation of Ferrocene: A Strong Dependence on the Concentration of the Supporting Electrolyte for Nonpolar Solvents. *The Journal of Physical Chemistry A* **2009,** *113* (7), 1259-1267.
13. Kosswattaarachchi, A. M.; Cook, T. R., Concentration-dependent charge-discharge characteristics of non-aqueous redox flow battery electrolyte combinations. *Electrochimica Acta* **2018,** *261*, 296-306.
14. Nutting, J. E.; Rafiee, M.; Stahl, S. S., Tetramethylpiperidine N-Oxyl (TEMPO), Phthalimide N-Oxyl (PINO), and Related N-Oxyl Species: Electrochemical Properties and Their Use in Electrocatalytic Reactions. *Chem Rev* **2018,** *118* (9), 4834-4885.
15. Yu, X.; Manthiram, A., Nonaqueous hybrid redox flow energy storage with a sodium–TEMPO chemistry and a single-ion solid electrolyte separator. *Energy Advances* **2022,** *1* (1), 21-27.
16. Tsunaga, M.; Iwakura, C.; Tamura, H., Electrode reactions of nitroxide radicals at platinum in acetonitrile. *Electrochimica Acta* **1973,** *18* (3), 241-245.

17. Wei, X.; Xu, W.; Vijayakumar, M.; Cosimbescu, L.; Liu, T.; Sprenkle, V.; Wang, W., TEMPO-based catholyte for high-energy density nonaqueous redox flow batteries. *Adv Mater* **2014,** *26* (45), 7649-53.
18. Alkhayri, F.; Dyker, C. A., Evaluation of Two-Electron Bispyridinylidene Anolytes and a TEMPO Catholyte for Non-Aqueous Redox Flow Batteries. *Journal of The Electrochemical Society* **2021,** *168* (7), 070501.
19. Zhou, W.; Liu, W.; Qin, M.; Chen, Z.; Xu, J.; Cao, J.; Li, J., Fundamental properties of TEMPO-based catholytes for aqueous redox flow batteries: effects of substituent groups and electrolytes on electrochemical properties, solubilities and battery performance. *RSC Advances* **2020,** *10* (37), 21839-21844.
20. Wylie, L.; Hakatayama-Sato, K.; Go, C.; Oyaizu, K.; Izgorodina, E. I., Electrochemical characterization and thermodynamic analysis of TEMPO derivatives in ionic liquids. *Phys Chem Chem Phys* **2021,** *23* (17), 10205-10217.
21. Liu, Y.; Goulet, M.-A.; Tong, L.; Liu, Y.; Ji, Y.; Wu, L.; Gordon, R. G.; Aziz, M. J.; Yang, Z.; Xu, T., A Long-Lifetime All-Organic Aqueous Flow Battery Utilizing TMAP-TEMPO Radical. *Chem* **2019,** *5* (7), 1861-1870.
22. Zhao, Y.; Zhang, J.; Agarwal, G.; Yu, Z.; Corman, R. E.; Wang, Y.; Robertson, L. A.; Shi, Z.; Doan, H. A.; Ewoldt, R. H.; Shkrob, I. A.; Assary, R. S.; Cheng, L.; Srinivasan, V.; Babinec, S. J.; Zhang, L., TEMPO allegro: liquid catholyte redoxmers for nonaqueous redox flow batteries. *Journal of Materials Chemistry A* **2021,** *9* (31), 16769-16775.
23. Martínez, L.; Andrade, R.; Birgin, E. G.; Martínez, J. M., PACKMOL: A package for building initial configurations for molecular dynamics simulations. *Journal of Computational Chemistry* **2009,** *30* (13), 2157-2164.
24. Abraham, M. J.; Murtola, T.; Schulz, R.; Páll, S.; Smith, J. C.; Hess, B.; Lindahl, E., GROMACS: High performance molecular simulations through multi-level parallelism from laptops to supercomputers. *SoftwareX* **2015,** *1-2*, 19-25.
25. Jorgensen, W. L.; Maxwell, D. S.; Tirado-Rives, J., Development and Testing of the OPLS All-Atom Force Field on Conformational Energetics and Properties of Organic Liquids. *Journal of the American Chemical Society* **1996,** *118* (45), 11225-11236.
26. Dodda, L. S.; Cabeza de Vaca, I.; Tirado-Rives, J.; Jorgensen, W. L., LigParGen web server: an automatic OPLS-AA parameter generator for organic ligands. *Nucleic Acids Res* **2017,** *45* (W1), W331-W336.
27. Doherty, B.; Zhong, X.; Gathiaka, S.; Li, B.; Acevedo, O., Revisiting OPLS Force Field Parameters for Ionic Liquid Simulations. *J Chem Theory Comput* **2017,** *13* (12), 6131-6145.
28. Barone, V.; Cossi, M., Quantum Calculation of Molecular Energies and Energy Gradients in Solution by a Conductor Solvent Model. *The Journal of Physical Chemistry A* **1998,** *102* (11), 1995-2001.
29. Klamt, A.; Schüürmann, G., COSMO: a new approach to dielectric screening in solvents with explicit expressions for the screening energy and its gradient. *J. Chem. Soc., Perkin Trans. 2* **1993,** (5), 799-805.
30. Frisch, M. J.; Trucks, G. W.; Schlegel, H. B.; Scuseria, G. E.; Robb, M. A.; Cheeseman, J. R.; Scalmani, G.; Barone, V.; Petersson, G. A.; Nakatsuji, H.; Li, X.; Caricato, M.; Marenich, A. V.; Bloino, J.; Janesko, B. G.; Gomperts, R.; Mennucci, B.; Hratchian, H. P.; Ortiz, J. V.; Izmaylov, A. F.; Sonnenberg, J. L.; Williams; Ding, F.; Lipparini, F.; Egidi, F.; Goings, J.; Peng, B.; Petrone, A.; Henderson, T.; Ranasinghe, D.; Zakrzewski, V. G.; Gao, J.; Rega, N.; Zheng, G.; Liang, W.; Hada, M.; Ehara, M.; Toyota, K.; Fukuda, R.; Hasegawa, J.; Ishida, M.; Nakajima, T.; Honda, Y.; Kitao, O.; Nakai, H.; Vreven, T.; Throssell, K.; Montgomery Jr., J. A.; Peralta, J. E.; Ogliaro, F.; Bearpark, M. J.; Heyd, J. J.; Brothers, E. N.; Kudin, K. N.; Staroverov, V. N.; Keith, T. A.; Kobayashi, R.; Normand, J.; Raghavachari, K.; Rendell, A. P.; Burant, J. C.; Iyengar, S. S.; Tomasi, J.; Cossi, M.; Millam, J. M.; Klene, M.; Adamo, C.; Cammi, R.; Ochterski, J. W.;

Martin, R. L.; Morokuma, K.; Farkas, O.; Foresman, J. B.; Fox, D. J. *Gaussian 16 Rev. A.03*, Wallingford, CT, 2016.
31. Li, Z.; Robertson, L. A.; Shkrob, I. A.; Smith, K. C.; Cheng, L.; Zhang, L.; Moore, J. S.; Z, Y., Realistic Ion Dynamics through Charge Renormalization in Nonaqueous Electrolytes. *The Journal of Physical Chemistry B* **2020,** *124* (15), 3214-3220.
32. Bussi, G.; Donadio, D.; Parrinello, M., Canonical sampling through velocity rescaling. *The Journal of Chemical Physics* **2007,** *126* (1), 014101.
33. Berendsen, H. J. C.; Postma, J. P. M.; van Gunsteren, W. F.; DiNola, A.; Haak, J. R., Molecular dynamics with coupling to an external bath. *The Journal of Chemical Physics* **1984,** *81* (8), 3684--3690.
34. Parrinello, M.; Rahman, A., Polymorphic transitions in single crystals: A new molecular dynamics method. *Journal of Applied Physics* **1981,** *52* (12), 7182-7190.
35. Wu, X.; Gong, Y.; Xu, S.; Yan, Z.; Zhang, X.; Yang, S., Electrical Conductivity of Lithium Chloride, Lithium Bromide, and Lithium Iodide Electrolytes in Methanol, Water, and Their Binary Mixtures. *Journal of Chemical & Engineering Data* **2019,** *64* (10), 4319-4329.
36. Shkrob, I. A.; Robertson, L. A.; Yu, Z.; Assary, R. S.; Cheng, L.; Zhang, L.; Sarnello, E.; Liu, X.; Li, T.; Preet Kaur, A.; Malsha Suduwella, T.; Odom, S. A.; Wang, Y.; Ewoldt, R. H.; Farag, H. M.; Z, Y., Crowded electrolytes containing redoxmers in different states of charge: Solution structure, properties, and fundamental limits on energy density. *Journal of Molecular Liquids* **2021,** *334*, 116533.
37. Endres, F., Physical chemistry of ionic liquids. *Phys Chem Chem Phys* **2010,** *12* (8), 1648.
38. Palmer, B. J., Transverse-current autocorrelation-function calculations of the shear viscosity for molecular liquids. *Phys Rev E Stat Phys Plasmas Fluids Relat Interdiscip Topics* **1994,** *49* (1), 359-366.
39. Hansen, J. S., Where is the hydrodynamic limit? *Molecular Simulation* **2021,** *47* (17), 1391-1401.
40. Wang, Y.; Kaur, A. P.; Attanayake, N. H.; Yu, Z.; Suduwella, T. M.; Cheng, L.; Odom, S. A.; Ewoldt, R. H., Viscous flow properties and hydrodynamic diameter of phenothiazine-based redox-active molecules in different supporting salt environments. *Physics of Fluids* **2020,** *32* (8), 083108.
41. Maginn, E. J.; Messerly, R. A.; Carlson, D. J.; Roe, D. R.; Elliot, J. R., Best Practices for Computing Transport Properties 1. Self-Diffusivity and Viscosity from Equilibrium Molecular Dynamics [Article v1.0]. *Living Journal of Computational Molecular Science* **2020,** *2* (1).
42. Hess, B., Determining the shear viscosity of model liquids from molecular dynamics simulations. *The Journal of Chemical Physics* **2002,** *116* (1).
43. Elgrishi, N.; Rountree, K. J.; McCarthy, B. D.; Rountree, E. S.; Eisenhart, T. T.; Dempsey, J. L., A Practical Beginner's Guide to Cyclic Voltammetry. *Journal of Chemical Education* **2018,** *95* (2), 197-206.
44. Nicholson, R. S., Theory and Application of Cyclic Voltammetry for Measurement of Electrode Reaction Kinetics. *Analytical Chemistry* **1965,** *37* (11), 1351-1355.
45. Suga, T.; Pu, Y.-J.; Oyaizu, K.; Nishide, H., Electron-Transfer Kinetics of Nitroxide Radicals as an Electrode-Active Material. *Bulletin of the Chemical Society of Japan* **2004,** *77* (12), 2203-2204.
46. Keith B. Oldham, C. G. Z., and Alan M. Bond, Measurement of Ultrafast Electrode Kinetics via Steady-State Voltammograms at Microdisc Electrodes. *J. Electroanal. Chem.* **1988,** *248*, 467-473.
47. J. Barthel, H.-J. G., R. Neueder, and A. Schmid, Electrolyte solutions for technology - new aspects and approaches. *Pure and Applied Chemistry 71* (9), 1705-1715.
48. Gong, K.; Fang, Q.; Gu, S.; Li, S. F. Y.; Yan, Y., Nonaqueous redox-flow batteries: organic solvents, supporting electrolytes, and redox pairs. *Energy & Environmental Science* **2015,** *8* (12), 3515-3530.
49. Tsierkezos, N. G.; Philippopoulos, A. I., Studies of ion solvation and ion association of n-tetrabutylammonium hexafluorophosphate and n-tetrabutylammonium tetraphenylborate in various solvents. *Fluid Phase Equilibria* **2009,** *277* (1), 20-28.
50. Wang, H.; Wang, J.; Zhang, S.; Pei, Y.; Zhuo, K., Ionic association of the ionic liquids [C4mim][BF4], [C4mim][PF6], and [Cnmim]Br in molecular solvents. *Chemphyschem* **2009,** *10* (14), 2516-23.

51. Socrates, G., *Infrared and Raman characteristic group frequencies : tables and charts / George Socrates*. Third edition.. ed.; Chichester : Wiley: Chichester, 2004.
52. Lawrence, C. P.; Nakayama, A.; Makri, N.; Skinner, J. L., Quantum dynamics in simple fluids. *J Chem Phys* **2004,** *120* (14), 6621-4.
53. Ramirez, R.; Lopez-Ciudad, T.; Kumar, P. P.; Marx, D., Quantum corrections to classical time-correlation functions: hydrogen bonding and anharmonic floppy modes. *J Chem Phys* **2004,** *121* (9), 3973-83.